drones

MDPI

Article

Aerodynamic Interference of Stratospheric Airship Envelope on Contra-Rotating Propellers

Guoquan Tao [1], Jizheng Zhang [2], Cong Xie [3,*], Long Jin [2], Bin Xiang [2] and Jialin Chen [2]

[1] Institute of Unmanned System, Beihang University, Beijing 100191, China
[2] School of Aeronautic Science and Engineering, Beihang University, Beijing 100191, China
[3] School of Materials Science and Engineering, Beihang University, Beijing 100191, China
* Correspondence: xiecong@buaa.edu.cn

Highlights

What are the main findings?

- The envelope of stratospheric airship causes interference in contra-rotating propellers, the extent of which differs with different relative positions of propellers and envelope.
- The thrust generated by a single propeller blade fluctuates periodically during rotation as distance to the envelope changes. This phenomenon is mainly observed when the propellers are positioned in the front part of the airship envelope.

What is the implication of the main finding?

- The position of the propeller relative to the airship envelope should be taken into account when designing the layout of the airship to improve propeller thrust and efficiency.
- Placing the propeller at the front and close to the envelope should be avoided because the periodic fluctuation of the thrust is significant and possibly detrimental.

Abstract

Contra-rotating propellers (CRPs) have promising applications in stratospheric airships. However, the aerodynamic interference caused by the airship envelope could lead to thrust loss, efficiency decrease, and even structure fatigue. This paper constructed parameterized computational fluid dynamic (CFD) models to simulate the aerodynamic performance of CRPs at different positions relative to the airship envelope. The total thrust, torque, efficiency, and thrust generated by a single propeller blade all show different degrees of interference. It is advised that such interference be considered in the layout design of stratospheric airships to improve propeller efficiency and ensure a longer structure fatigue life.

Keywords: stratospheric airship; CRP; CFD; aerodynamic interference

Check for updates

Academic Editor: Abdessattar Abdelkefi

Received: 11 December 2025
Revised: 23 January 2026
Accepted: 27 January 2026
Published: 28 January 2026

Copyright: © 2026 by the authors. Licensee MDPI, Basel, Switzerland. This article is an open access article distributed under the terms and conditions of the Creative Commons Attribution (CC BY) license.

1. Introduction

Stratospheric airships are airships designed to operate in the stratosphere, typically at an altitude of above 20 km [1,2]. With lift generated by buoyancy instead of aerodynamic forces, stratospheric airships have the potential to stay in continuous flight for months. Due to the long endurance and high operational altitude, stratospheric airships are able to perform tasks similar to satellites, such as communication relaying and remote sensing, but without the need of an orbital launch vehicle, significantly reducing operational cost.

The high altitude and long flight time of stratospheric airship pose new challenges to the design of propellers. Firstly, during long-term flight the vibration caused by the rotation of the propellers and motors puts a strain on the structures, leading to possible fatigue failure [3]. Secondly, compared to traditional airplanes, the body of an airship is an expansive surface close to the propellers, causing interference in airflow, which further amplifies the vibration [4]. Thirdly, because airships use buoyancy as lift, the generation of lift and thrust is decoupled, giving greater design freedom to the position and number of propellers of the propulsion system, which complicates the optimization process [5,6].

Contra-rotating propellers (CRPs) are two sets of coaxial propellers rotating in opposite directions at the same speed. CRP configuration improves efficiency by 1% to 16% [7], while the torque generated by the two propellers is canceled out. The application of CRP configuration on stratospheric airships is promising, yet rigorous aerodynamic and structural analysis is needed for such complex design.

Many studies were conducted on the design and test of propellers used on stratospheric airships. He et al. [8] conducted ground experiment on the propulsion system of a stratospheric airship but mainly focused on the design of electric motors. Chen, S. et al. [9] used the simulation method to design a propulsion system for high altitude airship, giving detailed performance predictions. Liu, P. et al. [10,11] designed a three-blade propeller for stratospheric airships, evaluated the performance of the propeller with strip theory, and verified the result with simulation and wind tunnel test. Wang et al. [12] used the simulation method to analyze the aerodynamic properties of a two-blade high-altitude propeller and verified the result with scaled wind tunnel tests. Liu, X. et al. [13] designed a stratospheric propeller and used different simulation methods to analyze the performance of the propeller. Xie et al. [14] proposed a performance prediction method for the design of a stratospheric propeller and used simulation methods to verify the feasibility of the method.

CRPs are a promising method of propulsion for stratospheric airships. Tang et al. [15] used the CFD method to analyze the aerodynamic performance of a CRP for stratospheric airship. Chen, Y. et al. [16] studied the performance of CRPs with different configurations using wind tunnel tests, concluding that CRP configuration is better than multiple single-propeller configurations or a single propeller with double the blade number. Xie et al. [17,18] discussed the influence of rotation speed and spacing of propellers on CRP performance, optimizing the design of CRP.

The investigation of aerodynamic interference on propellers is a field of research with practical importance. Hadipour et al. [19] investigated the thrust of propellers considering ground effects, with the tilt angle as a variable. Fei et al. [20] analyzed the influence of propellers to the pressure distribution on the airship, which leads to noticeable changes in the drag of the airship depending on the position of the propellers. Konuş et al. [21] found that propellers in close proximity of walls show a deviation of thrust vector. Chen et al. [22] noticed that the performance of propellers at different positions are influenced by the airship but mainly focused on case-specific results.

Previous research analyzed the performance and design process for stratospheric propellers, with some research considering the application of CRP on stratospheric airships. The interaction between airship and propellers are studied to optimize the layout of the propulsion system, but the main focus is on the drag of the airship caused by propellers and the general performance of the propellers. More research are needed to analyze the influence of the airship on the drag, torque, efficiency, and vibration of propellers, as well as the implications of these effects for the overall layout design.

In this paper, a parameterized airship–propeller interaction CFD model is constructed. The accuracy of this model is verified with different cell counts and time step numbers. Using this model, the performance of a set of CRP without the airship envelope is analyzed

as a baseline. The performance of CRP at different positions relative to the airship envelope is also analyzed for comparison. The thrust of a single propeller blade is analyzed to better describe the aerodynamic interference of the airship envelope. In the end, the property of the envelope interference is described, and the possible implication of such interference on airship layout design is given.

2. Airship–Propeller Interaction Model

2.1. Simulation Method

2.1.1. Finite Volume Method

In this paper, the model contains a compound of the airship envelope and a pair of contra-rotating propellers. In order to obtain detailed information on the unsteady flow in the model, especially the envelope interference on the propeller blades at different rotation angles, transient simulation is necessary. Finite volume method (FVM) was used to solve the simulation problem [23–25].

FVM is strictly conservative, which is important to ensure the accuracy of flow simulation. FVM can be implemented on unstructured meshes, which makes mesh drawing easier to automate, allowing more complicated model geometry and parameterization of model design. FVM allows easy integration of various boundary conditions, since the unknown variables are evaluated at the centroids of the volume elements instead of on the boundary faces.

The conservation equation of a general property ϕ (e.g., temperature, mass) can be written as:

$$\underbrace{\frac{\partial(\rho\phi)}{\partial t}}_{\text{transient term}} + \underbrace{\nabla\cdot(\rho\mathbf{v}\phi)}_{\text{convective term}} = \underbrace{\nabla\cdot\left(\Gamma^{\phi}\nabla\phi\right)}_{\text{diffusion term}} + \underbrace{Q^{\phi}}_{\text{source term}} \tag{1}$$

where ρ is the density of the fluid, V and S are the volume and surface area of the control volume, and $\rho\mathbf{v}\phi$ is the transport of ϕ by the fluid flow. Γ^{ϕ} is a coefficient representing the diffusion effect of ϕ. Q^{ϕ} is the generation/destruction of ϕ within the control volume per unit volume.

The above equation is integrated over the volume elements of the divided domain; for transient analysis, the equation is also integrated over time.

$$\begin{aligned}\int_{t}^{t+\Delta t}\int_{Vc}\frac{\partial(\rho\phi)}{\partial t}dVdt + \int_{t}^{t+\Delta t}\left[\sum_{f\sim nb(C)}\left(\int_{f}(\rho\mathbf{v}\phi)_{f}\cdot d\mathbf{S}\right)\right]dt = \\ \int_{t}^{t+\Delta t}\left[\sum_{f\sim nb(C)}\left(\int_{f}(\Gamma\nabla\phi)_{f}\cdot d\mathbf{S}\right)\right]dt + \int_{t}^{t+\Delta t}\left[\int_{f}\left(Q^{\phi}\right)\cdot dV\right]dt\end{aligned} \tag{2}$$

2.1.2. SST k-ω Model

This paper employs the shear-stress transport (SST) k-ω turbulence model. As a two-equation model, a switching function is utilized to solve k-ω model in the inner part of the boundary layer and gradually switch to k-ε model in the outer layer. The SST k-ω model improves the baseline k-ω model by accounting for the effect of turbulent shear-stress. This turbulence model is well documented and verified by previous studies [26,27] and can provide accurate results in a wide variety of flow problems, especially under adverse pressure gradient conditions.

2.2. Model Setup

2.2.1. Workflow

To compare the performance of the CRP at different relative positions of the envelope, parameterized models are constructed with two parameters to define the position of CRP.

The simulation conditions are the same across all models and are derived according to the typical flight altitude and airspeed of a stratospheric airship. Steady state simulations are first conducted to serve as the initial state of the transient simulations. The transient simulations are conducted for a more detailed flow field reflecting the rotation of the propellers. The diagram of the simulation workflow is presented in Figure 1.

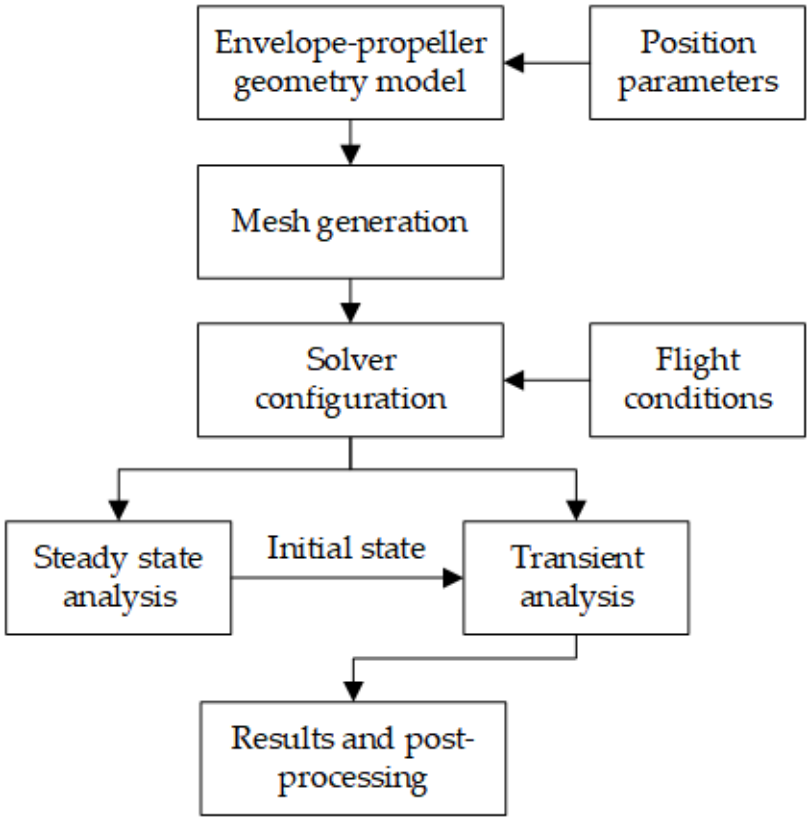


Figure 1. Simulation workflow of airship–propeller interaction model.

2.2.2. Envelope and Propeller Design

The envelope of the airship is based on the LOTTE airship [28,29]. The generatrix of the airship envelope can be obtained from Equation (3) with a total length of 50 m (L = 50 m).

$$\begin{cases} \overline{y}(\overline{x}) = c\sqrt{\overline{x}},\ 0 < \overline{x} < 0.08 \\ \overline{y}(\overline{x}) = c_0 + c_1\overline{x} + c_2\overline{x}^2 + c_3\overline{x}^3 + c_4\overline{x}^4 + c_5\overline{x}^5,\ 0.08 < \overline{x} < 1 \end{cases} \quad (3)$$

$$\overline{x} = x/L,\ \overline{y} = y/L \quad (4)$$

The CRP configuration is shown in Figure 2. There are two propellers in a set of CRPs, rotating at the same rotational speed (n). The rotating vector of the front propeller points forward, while the aft propeller points backward. Both of the propellers share the same diameter (D), with 4 blades each. The distance between the front and aft propellers is 1.0 m (h = 1.0 m). Each propeller blade is labeled, with front propeller blades labeled as Fb1~Fb4 and aft propeller blades as Ab1~Ab4.

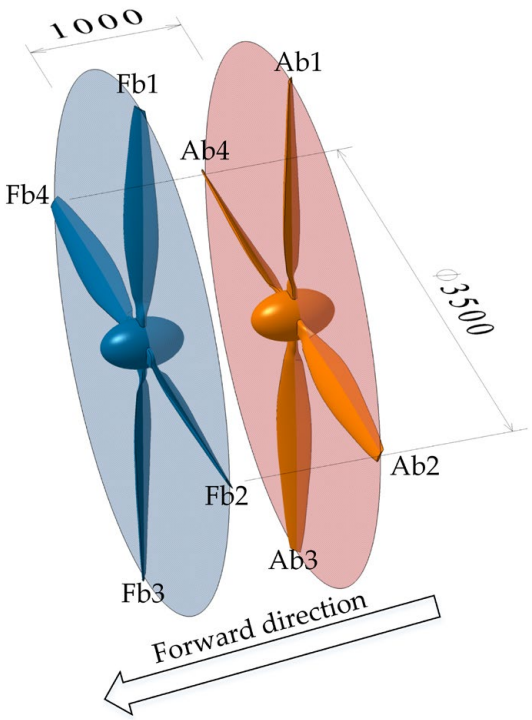


Figure 2. Contra-rotating propellers configuration, where the blue propeller is the front propeller, and the orange propeller is the aft propeller.

Two sets of CRPs are positioned symmetrically on each side of the envelope. The position of the CRPs are determined by the distance from the center of the two propellers to the bow of the envelope (x) and the distance from the tip of the blade to the envelope (d), as shown in Figure 3. Two parameters a and b can be obtained from the equation for simplified representation of the longitudinal and lateral position of the CRPs.

$$a = x/L,\ b = d/D \tag{5}$$

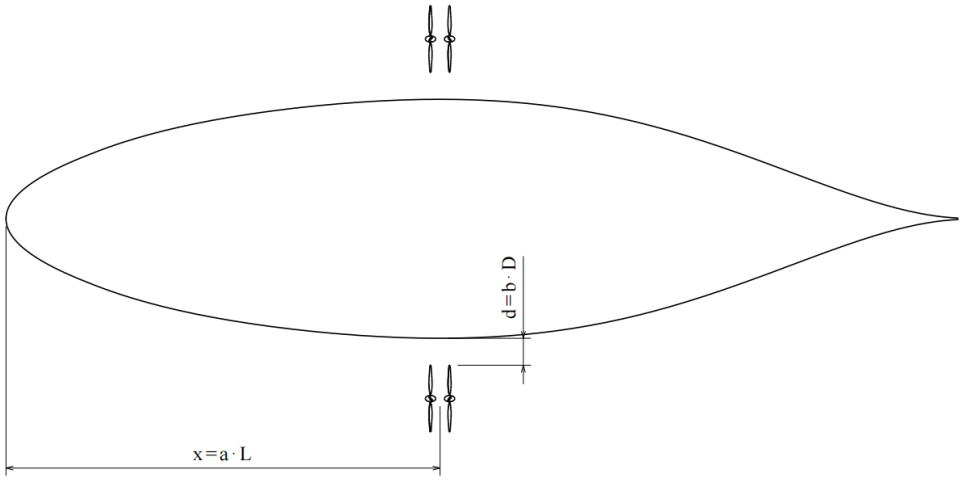


Figure 3. Airship envelope and the position of propellers.

Table 1 shows the parameters used to describe the airship model.

Table 1. Airship parameters.

Parameter	Value
generatrix coefficient (c)	0.2277
generatrix coefficient 0 (c_0)	0.0197
generatrix coefficient 1 (c_1)	0.7184
generatrix coefficient 2 (c_2)	−2.375
generatrix coefficient 3 (c_3)	5.0166
generatrix coefficient 4 (c_4)	−5.834
generatrix coefficient 5 (c_5)	2.4551
envelope length (L)	50.0 m
propeller diameter (D)	3.5 m
propeller rotation rate (n)	500 rpm
propeller distance (h)	1.0 m

The model used in aerodynamic analysis is a half model, as shown in Figure 4.

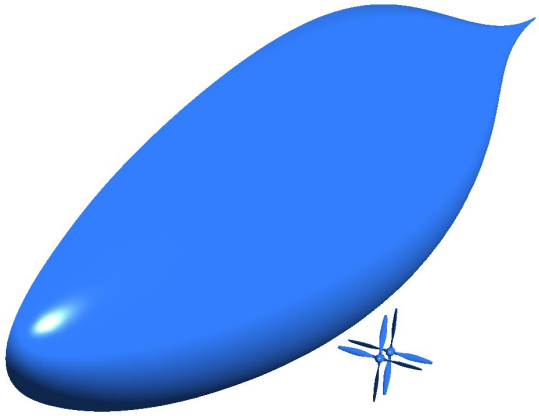


Figure 4. Half model of CRP and airship envelope (a = 0.20, b = 0.4).

The model is divided into 3 flow fields: 1 outer field and 2 propeller fields. The propeller fields are cylinder flow fields each containing a propeller. In simulation, the entirety of each propeller field is in rotation to simulate the rotation of the propeller, as shown in Figure 5. The outer field is 300 m × 100 m × 109.425 m in size, large enough to contain the entire model and reduce the effect of flow field boundary.

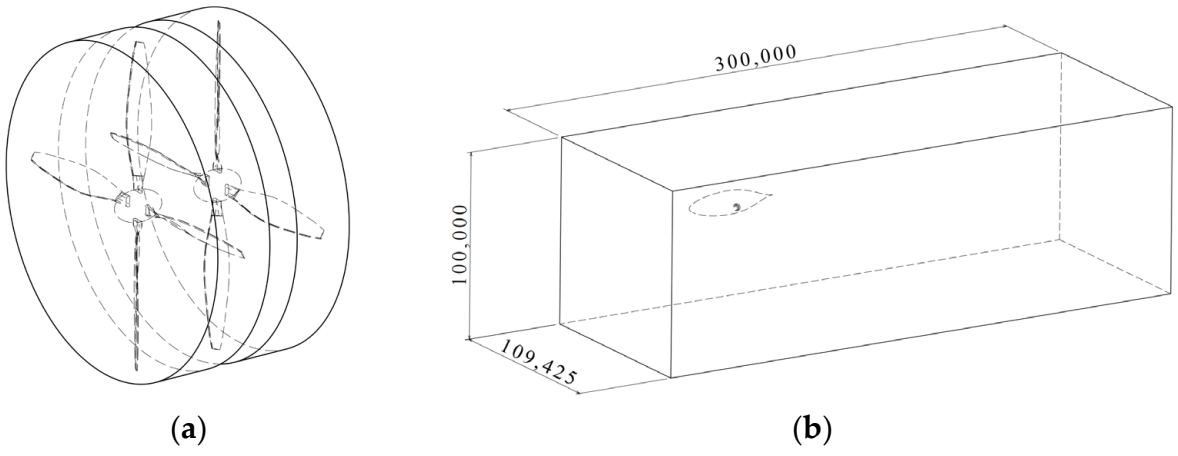


Figure 5. Flow field configuration: (**a**) propeller fields; (**b**) outer field.

In order to analyze the influence of the airship envelope on CRPs, models with CRPs at different positions are developed. A coordinate system including the longitudinal position

parameter a and lateral position parameter b is used to represent the different positions of CRPs relative to the airship envelope (e.g., a = 0.20 and b = 0.4 mean that the CRP is at 20% the total length of the envelope, and the distance between the envelope and the propeller blade tip is 40% the diameter of the propeller). A total of 3 longitudinal position parameters are chosen: a = [0.20, 0.45, 0.60]. The generatrix function of the envelope reaches its maximum at a = 0.45. A total of 7 lateral positions are chosen: b = [0.4, 0.7, 1.0, 1.3, 2.3, 3.4, 4.6]. There are more design points with smaller b because the change in performance is more drastic when the CRP is placed closer to the envelope. A total of 21 models are analyzed.

2.2.3. Mesh Generation

The meshes of the model are mainly unstructured grids with structured grids near the boundaries, as shown in Figure 6. The meshes close to the surfaces of the envelope and propellers are more refined to fit the geometry of the surfaces and capture the boundary layer of the flow.

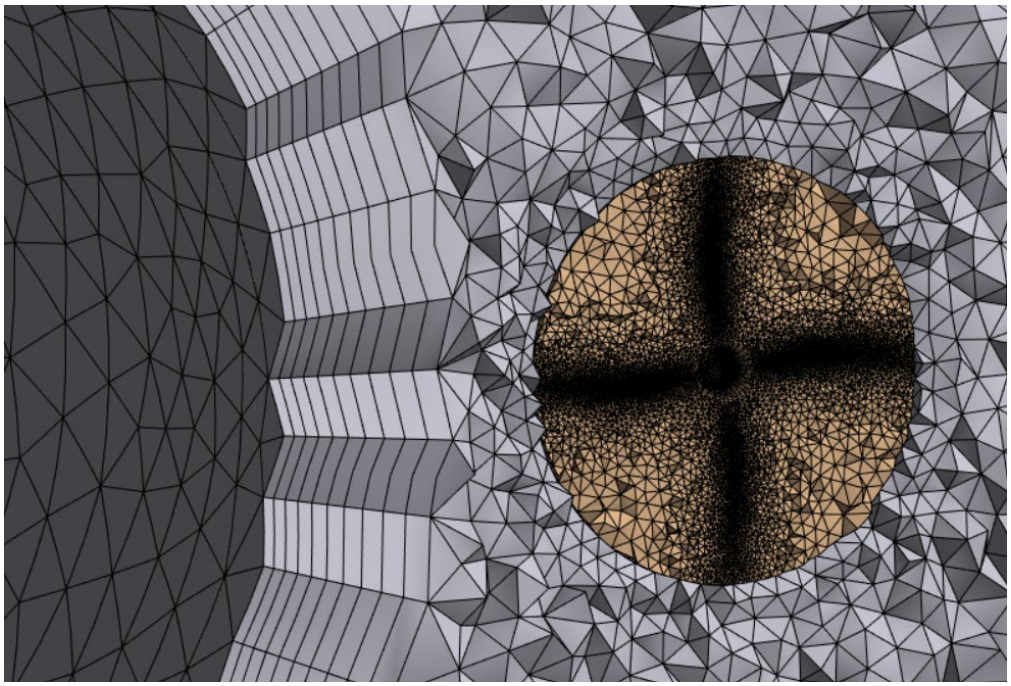


Figure 6. Mesh generated close to the propeller.

The rotational movement of the propeller fields means the meshes between fields cannot be connected. In order to transfer the flow information from the rotating propeller fields to the static outer field, a sliding mesh technique is adopted; the schematics of the method are shown in Figure 7. In this technique, fields are connected trough interfaces. When the fluid flow enters the sliding meshes from the static meshes across the interface, the flow information is transferred through a reference frame transformation. A reverse transformation is performed when the flow exits the sliding meshes into the static meshes. Note that meshes on both side of the interface are not always aligned and could be of different sizes, so additional interpolation procedures are needed to ensure accurate information transformation across the flow fields. The sliding mesh technique is verified by previous research and widely adopted in practice [30–33].

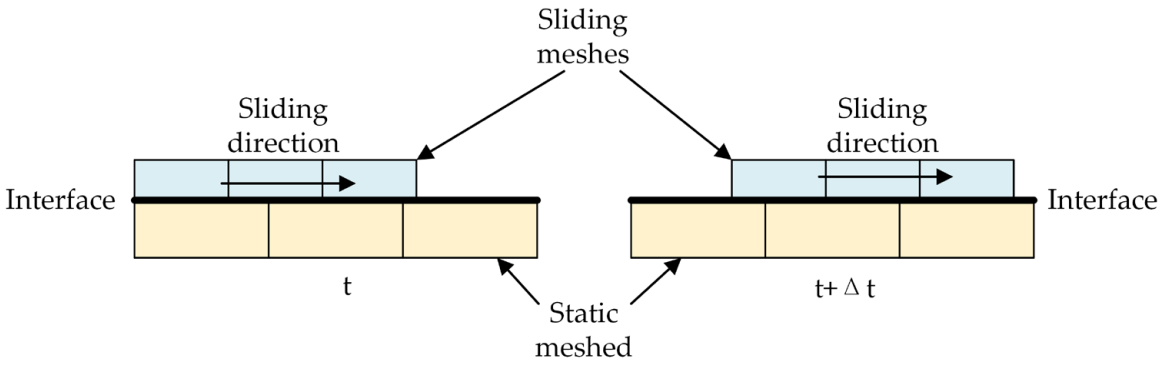


Figure 7. Side view example of sliding meshes.

2.2.4. Flight Conditions

Stratospheric airships operate at an altitude of around 20 km, with a cruise speed of less than 30 m/s. In this paper, an altitude of 19 km and a cruise speed of 20 m/s are chosen to represent a typical stratospheric airship.

Based on the U.S. standard atmosphere [34], the temperature, static pressure, density, and viscosity of the air can be interpolated given the altitude. The fluid parameters used for the simulations in this paper are shown in Table 2.

Table 2. Fluid parameters.

Parameter	Value
altitude (H)	19 km
airflow speed (V)	20 m/s
temperature (T)	216.7 K
air density (ρ)	0.1040 kg/m^3
air pressure (P)	6467 Pa
dynamic viscosity (μ)	1.422×10^{-5} kg/(m·s)

3. Model Accuracy Verification

In order to verify the grid quality of the aerodynamic model, models with different cell counts are compared. These models all have propellers in the same position (a = 0.20, b = 0.4). The thrust of the front propeller in each model is compared, as shown in Figure 8.

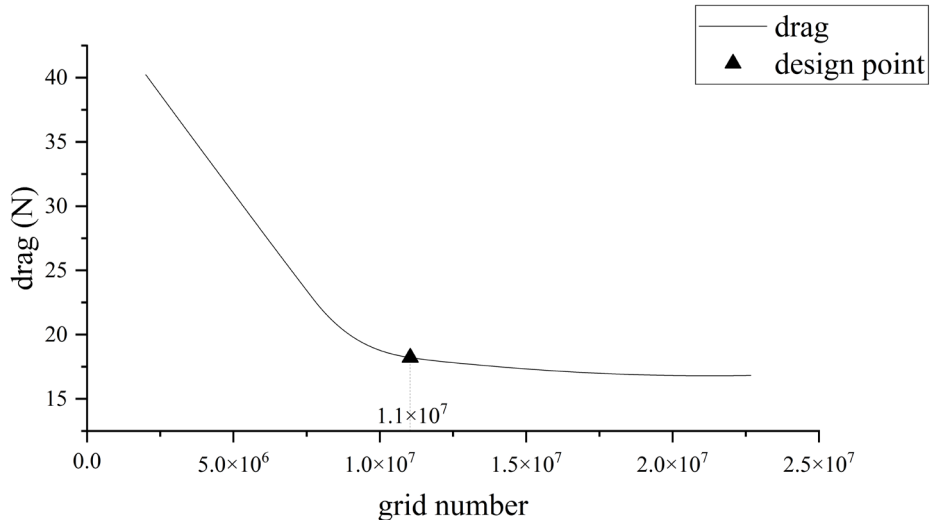


Figure 8. Front propeller aerodynamic drag with different model grid numbers.

The accuracy of the model is improved as cell count increases, but a cell count of more than 1.0×10^7 yields diminished return. A cell count of 1.1×10^7 is chosen for the models in this paper.

Each time step is 6.67×10^{-4} s long so that the propeller (rotating at 500 rpm) turns 2° every time step, capturing the detailed rotation movement of the propellers. The influence of the total time step on result accuracy is also analyzed, as shown in Figure 9.

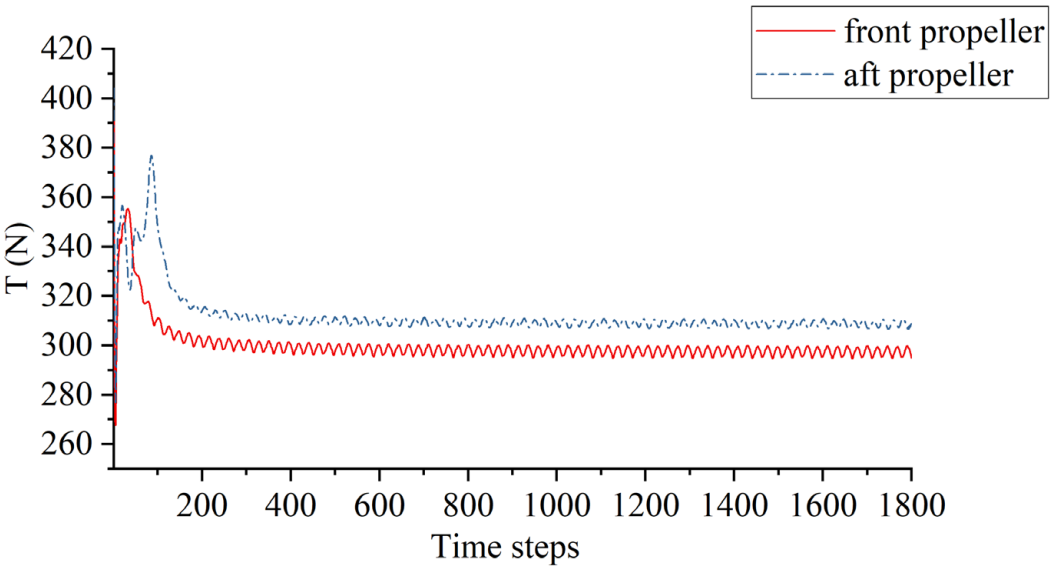


Figure 9. Front and aft propeller aerodynamic thrust (T) as time step increases.

Aerodynamic forces fluctuate drastically within the first 200 time steps, and later gradually converge to a state of periodic vibration with a frequency of 66.7 Hz, which is 8 times the rotation rate of the propeller. Considering the two propellers overlap 8 times in one rotation, this vibration frequency should be an accurate result of propeller overlap interference. Previous research also observed such interference [35,36]. The overlap interference can also be observed in propeller torque, propeller efficiency, and thrust of individual blades later in this paper.

Balancing computational time and model accuracy, a cell count of 1.1×10^7 is adopted, the length of each time step is 6.67×10^{-4} s, and simulation results are taken after 360 time steps, as shown in Table 3.

Table 3. Grid number and time step parameters.

Parameter	Value
grid number	1.1×10^7
time step length	6.67×10^{-4} s
time step number	>360

The propeller in this paper used a similar design with the 2-blade high-altitude propeller in [12], which can be scaled down using the similarity theorem and used as a benchmark to verify the accuracy of the CFD model in this paper.

The reference propeller and the scaled propeller are labeled as P1 and P2. The scale factor of their design parameters can be expressed as:

$$\lambda_i = \frac{i_{P1}}{i_{P2}}, i = [D, n, \mu, T] \quad (6)$$

where design parameters D, n, μ, and T are the propeller diameter, propeller rotation rate, dynamic viscosity, and thrust.

According to the similarity theorem, the Reynolds number should stay the same:

$$\frac{\mathrm{Re}_{P1}}{\mathrm{Re}_{P2}} = \frac{\frac{\rho_{P1} v_{P1} D_{P1}}{\mu_{P1}}}{\frac{\rho_{P2} v_{P2} D_{P2}}{\mu_{P2}}} = 1 \tag{7}$$

where Re is the Reynolds number of the propeller, ρ is the air density, and v is the blade tip velocity.

The scale factor of thrust can be obtained with:

$$\lambda_T = \frac{T_{P1}}{T_{P2}} = \frac{\rho_{P1} V_{P1}^2 D_{P1}^2}{\rho_{P2} V_{P2}^2 D_{P2}^2} = \frac{\mathrm{Re}_{P1} \mu_{P1} v_{P1} D_{P1}}{\mathrm{Re}_{P2} \mu_{P2} v_{P2} D_{P2}} = \frac{\mu_{P1} n_{P1} D_{P1}^2}{\mu_{P1} n_{P1} D_{P2}^2} = \lambda_\mu \lambda_\mathrm{n} \lambda_D^2 \tag{8}$$

The thrust of the scaled propeller can be obtained as:

$$T_{P2} = \frac{T_{P1}}{\lambda_T} = \frac{T_{P1}}{\lambda_\mu \lambda_\mathrm{n} \lambda_D^2} \tag{9}$$

Considering there are twice the number of blades in the scaled propeller, the benchmark thrust should be doubled. The parameters comparison of the reference propeller and the scaled propeller are shown in Table 4.

Table 4. Propeller parameters comparison.

Parameter	Reference Propeller	Scaled Propeller
blade number	2	4
propeller diameter (D)	8 m	3.5 m
propeller rotation rate (n)	200 rpm	500 rpm
dynamic viscosity (μ)	1.417×10^{-5} kg/(m·s)	1.422×10^{-5} kg/(m·s)
thrust (T)	342.3 N	328.7 N

The CFD result in this paper indicates that the thrust of the front propeller is 319.8 N, and the thrust of the aft propeller is 331.0 N. Therefore, the simulation result of the CFD model is reasonably close to the wind tunnel test result.

4. Performance Analysis of Contra-Rotating Propellers Without Envelope

A CRP model without the interference of airship envelope is analyzed as a baseline. The thrust curves of both front and aft propellers are shown in Figure 10, with the thrust curves of a model, with envelope at a = 0.20 and b = 0.4 added for comparison.

The aft propeller generates more thrust than the front propeller. The thrust fluctuates periodically at a frequency of 66.7 Hz. As analyzed in Section 3, this is caused by the overlap of front and aft propeller blades.

The thrust curves of each blade at different rotation angles are shown in Figure 11, with the thrust curves of each blade of a model, with envelope at a = 0.20 and b = 0.4 added for comparison.

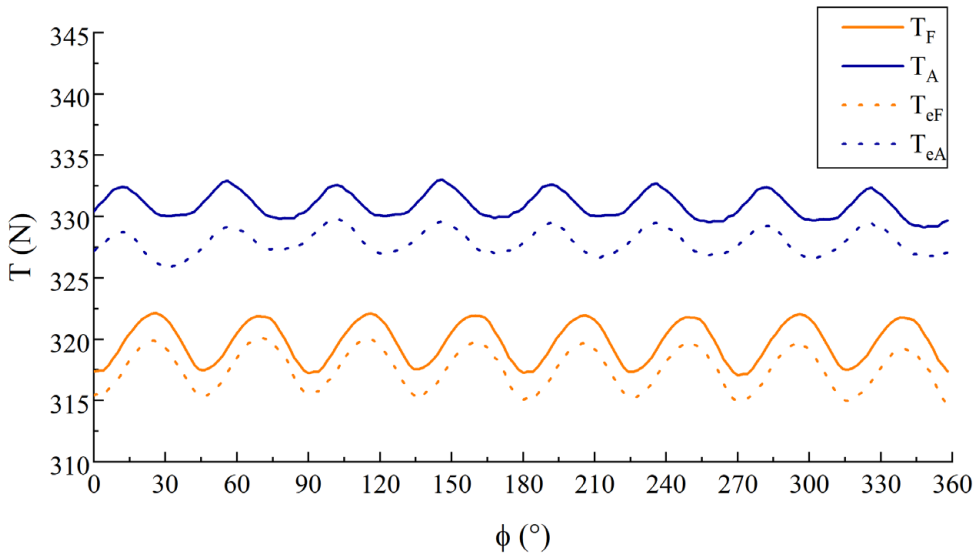


Figure 10. Front and aft propeller thrust in the model without envelope (T_F and T_A) and in the model with envelope at a = 0.20, b = 0.4 (T_{eF} and T_{eA}) at different rotation angles (ϕ).

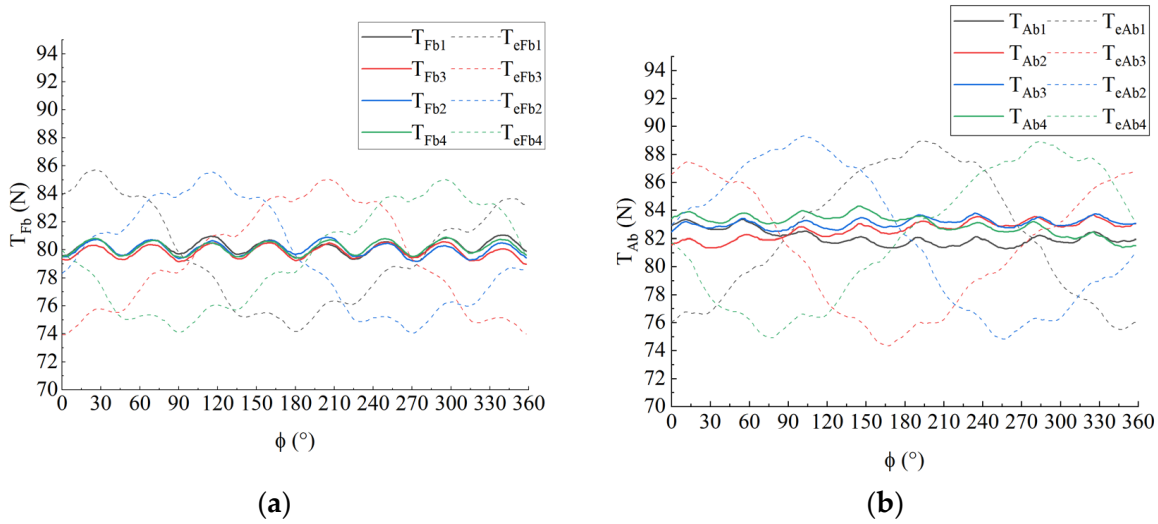


Figure 11. Propeller thrust of each blade at different rotation angles (ϕ): (**a**) thrust of the front propeller blades without envelope (T_{Fb1}~T_{Fb4}) and with envelope at a = 0.20, b = 0.4 (T_{eFb1}~T_{eFb4}); (**b**) thrust of the aft propeller blades without envelope (T_{Ab1}~T_{Ab4}), and with envelope at a = 0.20, b = 0.4 (T_{eAb1}~T_{eAb4}).

Both front and aft propellers show signs of overlap interference as mentioned in Section 3, with a frequency of 66.7 Hz. The thrust of each front propeller blade is mostly the same. The thrust of each aft propeller shows more fluctuation due to the flow turbulence behind the front propeller but shows the same periodic overlap interference. The fluctuation caused by turbulence is insignificant, as it is only about 3% of the thrust and does not change the trend in the curve of the total thrust of the aft propeller. This result is meaningful as a baseline to show the influence of the airship envelope later in Section 6.

The torque of both propellers are shown in Figure 12, with the torque of a model, with envelope at a = 0.20 and b = 0.4 added for comparison.

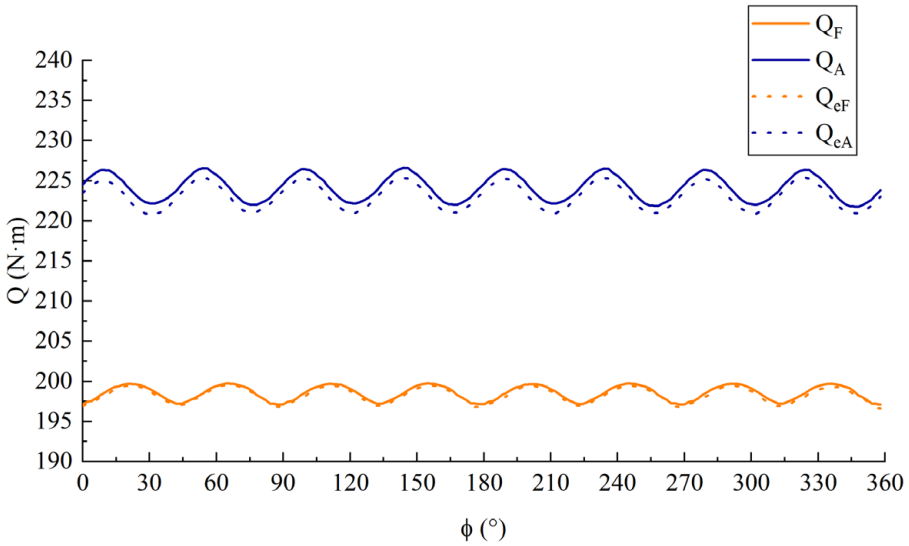


Figure 12. Front and aft propeller torque in the model without envelope (Q_F and Q_A) and in the model with envelope at a = 0.20 and b = 0.4 (Q_{eF} and Q_{eA}) at different rotation angles (ϕ).

The torque curve is similar to the thrust curve, with periodic overlap interference and larger torque in the front propeller. These results are used to calculate energy efficiency to better understand the performance of propellers.

The efficiency of both propellers are shown in Figure 13, with the efficiency of a model with envelope at a = 0.20 and b = 0.4 added for comparison. Efficiency is obtained through Equation (10), indicating the proportion of the work performed by thrust to the power needed for the rotation of the propeller.

$$\eta = \frac{TV}{Q\omega} \tag{10}$$

where T, V, Q, and ω are the thrust, airspeed, torque, and angular speed of the propeller, respectively.

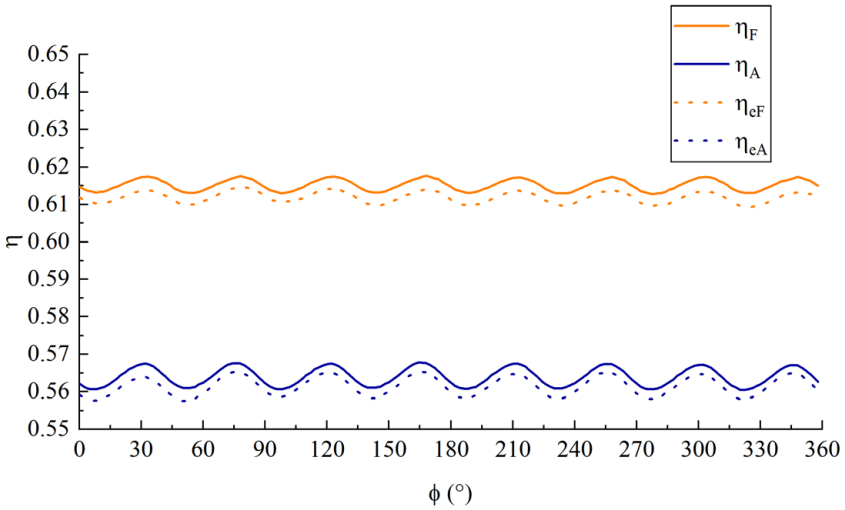


Figure 13. Front and aft propeller efficiency in the model without envelope (η_F and η_A) and in the model with envelope at a = 0.20 and b = 0.4 ($\overline{\eta}_F$ and $\overline{\eta}_A$) at different rotation angles (ϕ).

While the aft propeller generates more thrust, it is less efficient than the front propeller. The overlap interference can also be observed in the efficiency curve of both propellers.

5. Interference Analysis of Contra-Rotating Propellers with Envelope

As described in the simulation setup, there are 21 airship–propeller interaction models with CRPs at different relative positions to the envelope. Figure 14 shows the pressure contours of 12 models where propellers are relatively closer to the envelope (a = [0.20, 0.45, 0.60], b = [0.4, 0.7, 1.0, 1.3]). Figure 15 shows the streamlines that pass through the propellers in each model. Figure 16 shows the detailed pressure distribution on the propellers and streamlines that pass through the propellers.

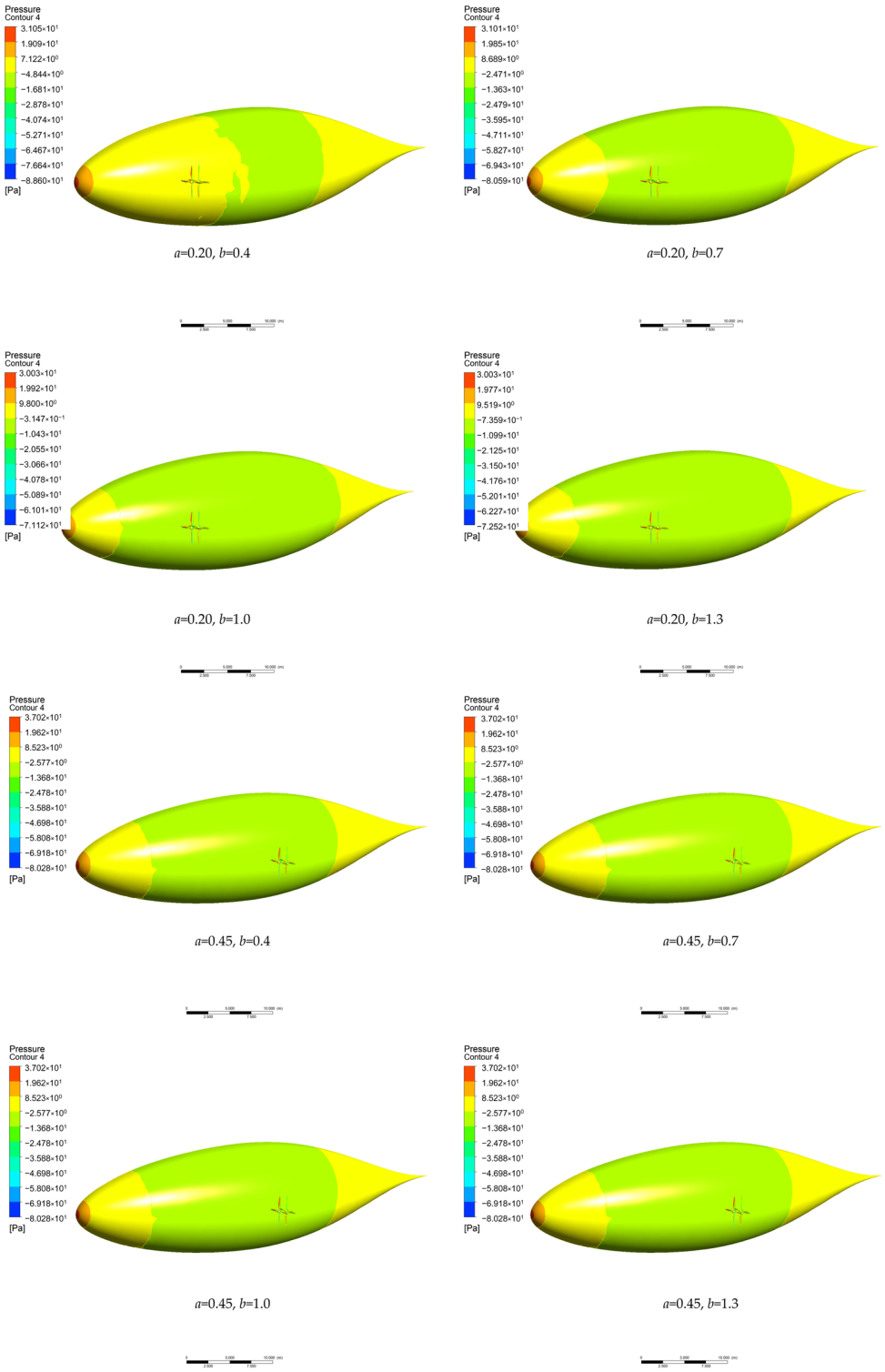


Figure 14. *Cont.*

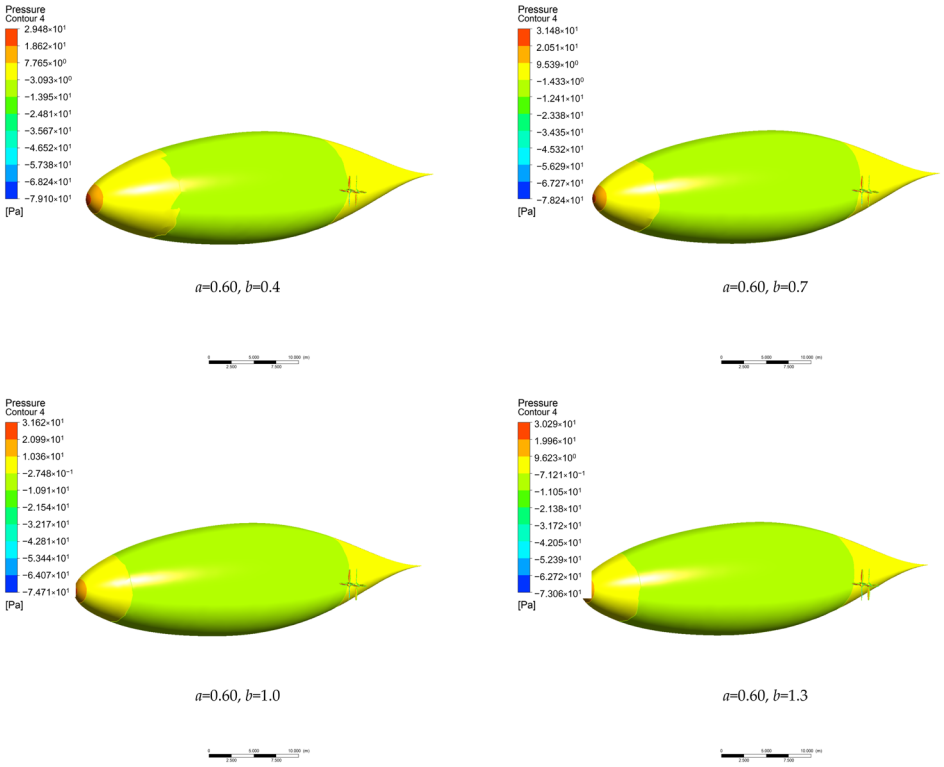


Figure 14. Pressure contours of airship–propeller interaction models, with propellers at different longitudinal positions *a* and lateral positions *b*.

The closer the propellers are to the envelope, the more interference there is, causing more drastic changes in the direction of the streamlines.

The thrust, torque, and efficiency of the propellers are compared. Figure 17 shows the total thrust of the propellers at different positions.

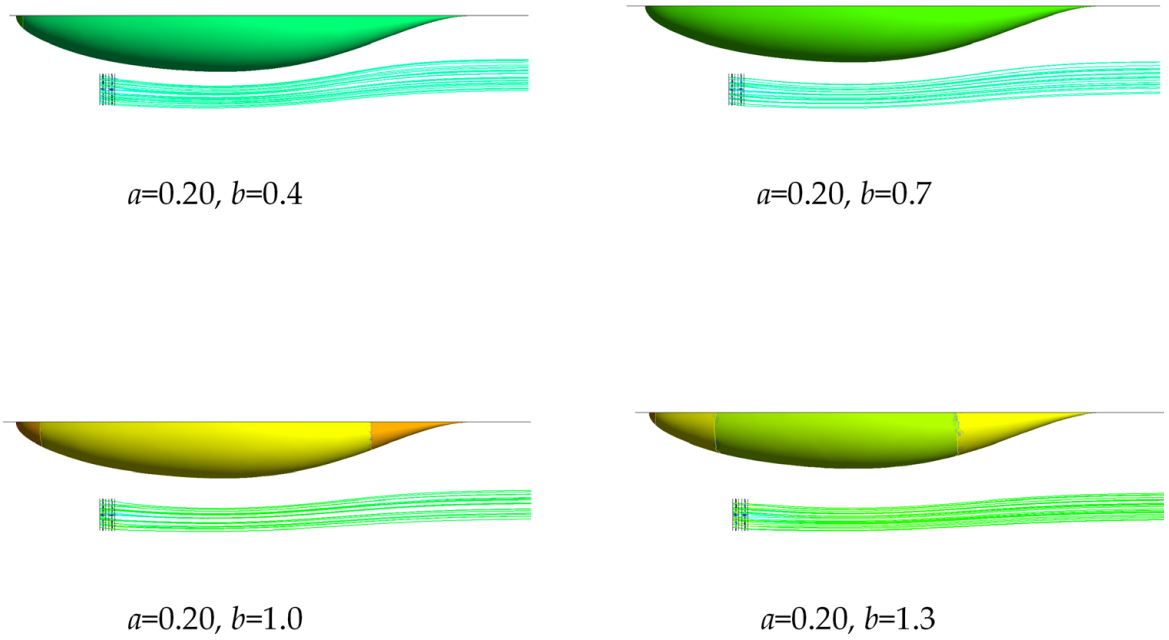


Figure 15. *Cont.*

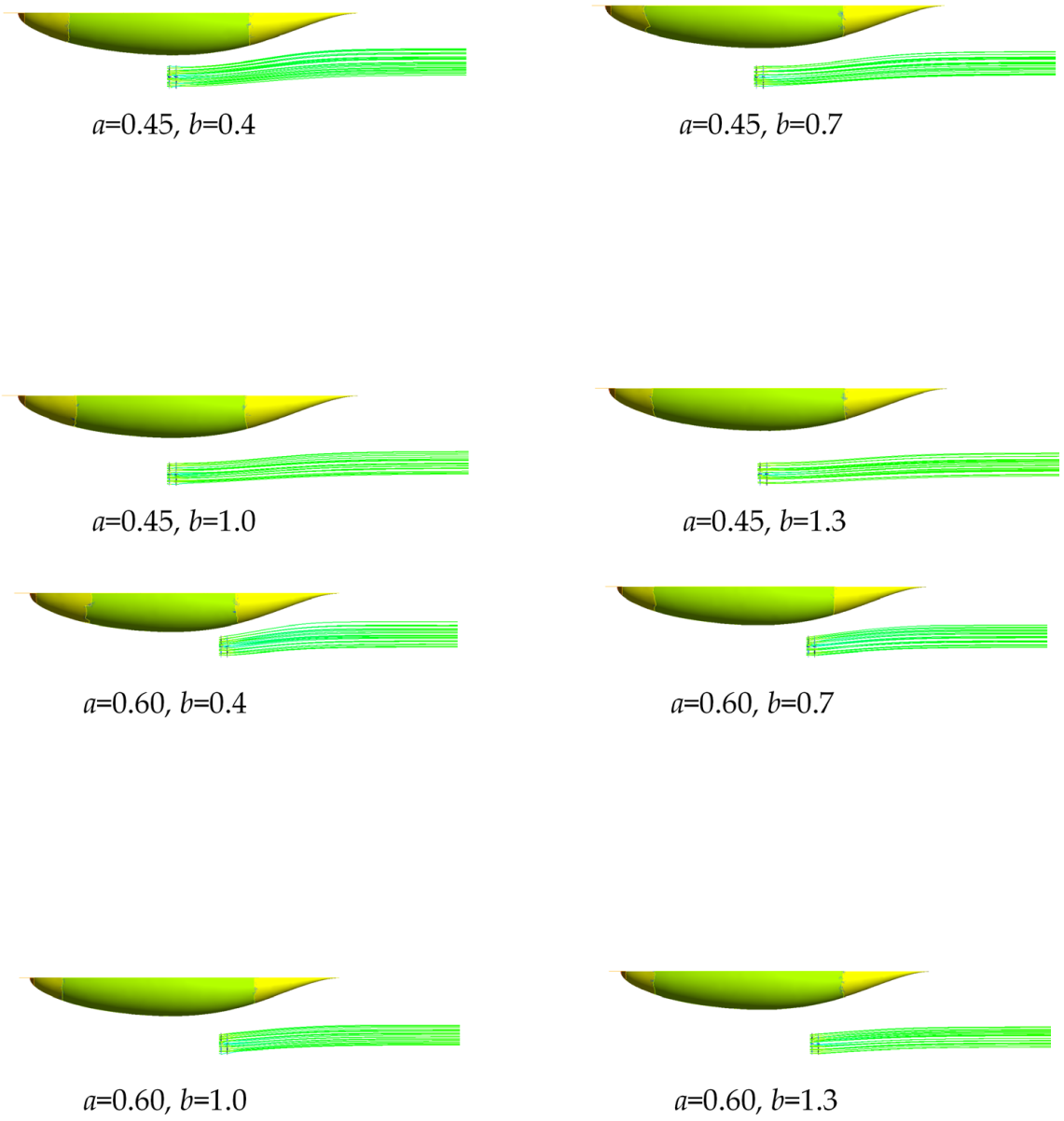


Figure 15. Streamlines that pass through the propellers in airship–propeller interaction models, with propellers at different longitudinal positions a and lateral positions b.

Same with baseline CRPs, the thrust of the front propeller is lower than that of the aft propeller. Propellers positioned at the front part of the envelope (a = 0.20) show little sign of envelope interference, and the thrust remains relatively the same at different lateral distances (b = 0.4~4.6). Meanwhile, the propellers at the middle part and rear part of the envelope (a = 0.45 and a = 0.60) show more significant envelope interference. The closer the propeller is to the envelope, the lower the thrust. The interference is stronger when the propeller is at the middle part, with a more drastic change in thrust than other positions.

The torque of the front and aft propellers at different positions is shown in Figure 18.

The torque curve is similar to the thrust curve, showing similar interference caused by the envelope.

The efficiency of the propellers is calculated with Equation (10), representing the ratio of the work performed by the thrust to the power needed for the rotation of the propeller. Figure 19 shows the efficiency of the front propeller in each model.

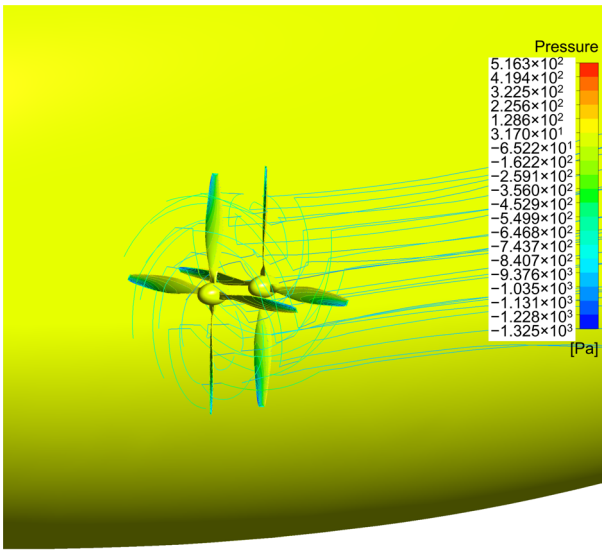


Figure 16. Pressure contour of the propellers and streamlines that pass through the propellers at positions a = 0.20 and b = 0.4.

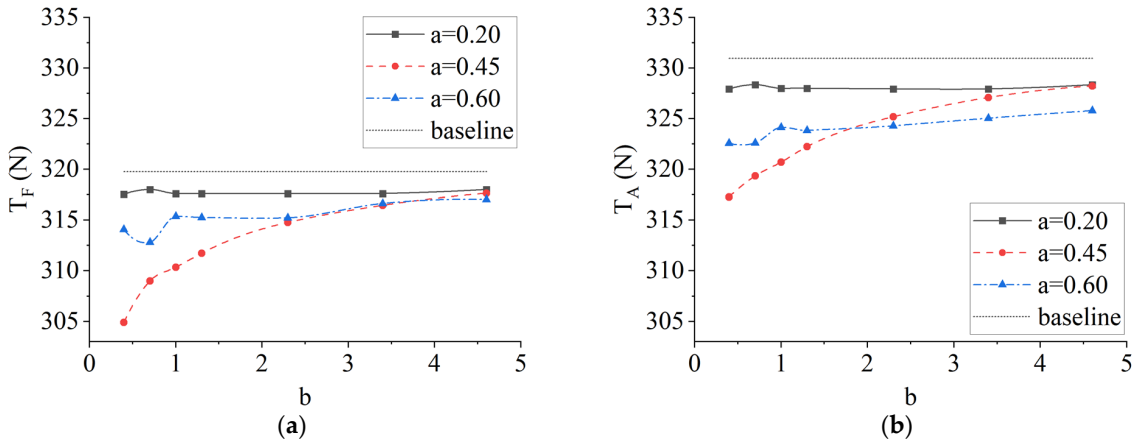


Figure 17. Propeller thrust at different longitudinal positions a, lateral positions b, and baseline model (without envelope): (**a**) front propeller thrust T_F; (**b**) aft propeller thrust T_A.

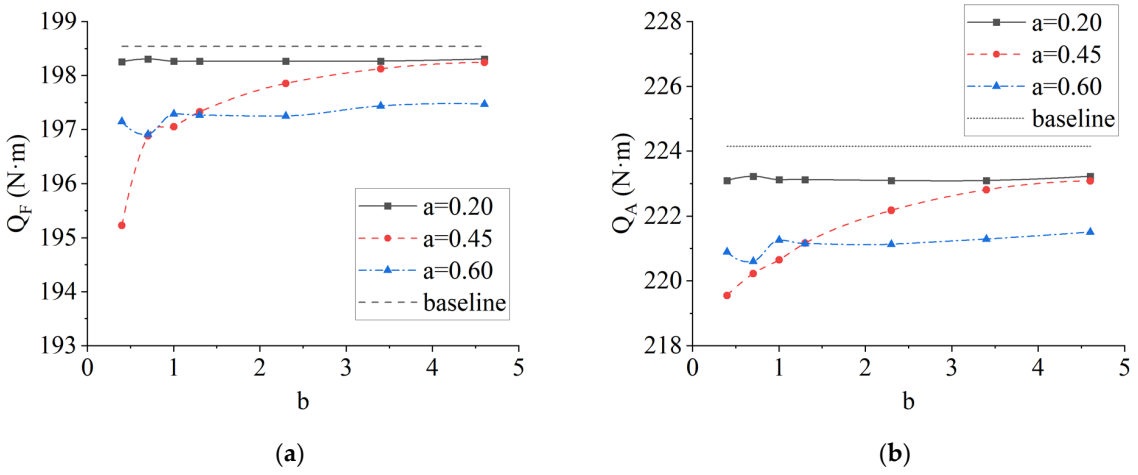


Figure 18. Front propeller torque at different longitudinal and lateral positions (a and b) and baseline model (without envelope): (**a**) front propeller torque; (**b**) aft propeller torque.

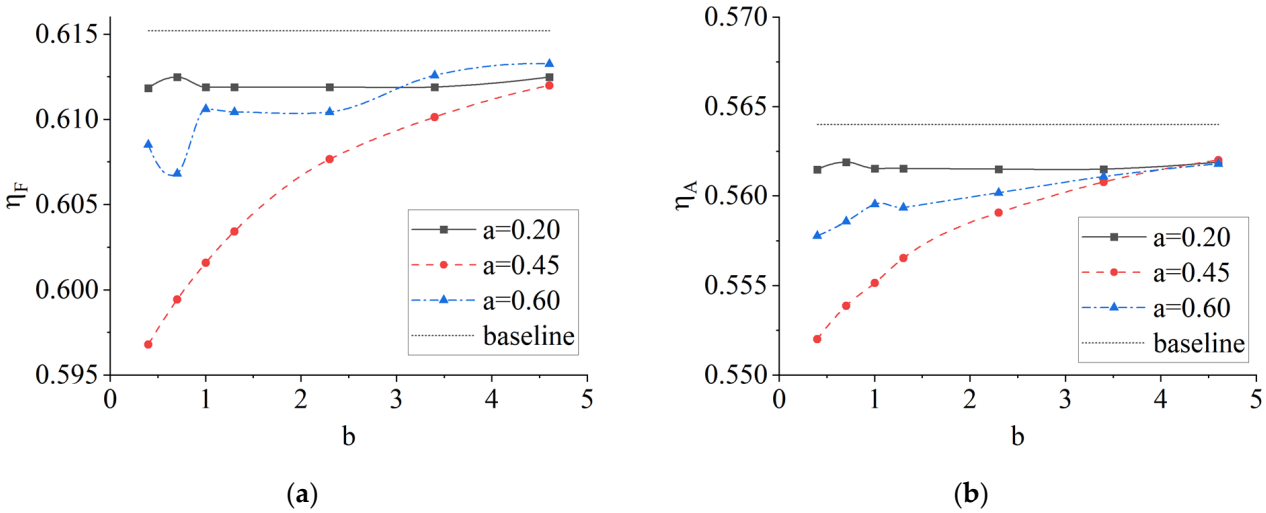


Figure 19. Front propeller efficiency at different longitudinal and lateral positions (*a* and *b*) and baseline model (without envelope): (**a**) front propeller efficiency; (**b**) aft propeller efficiency.

Efficiency shows similar trends as the thrust and torque of the propellers. Similar to the CRP without envelope interference, the aft propeller generates more thrust but is less efficient than the front propeller.

Although the envelope can interfere with CRP overall performance, the change in both thrust and efficiency is minimal (less than 5 N thrust and less than 2% efficiency). Therefore, more consideration should be put into the vibration of propeller blades as will be discussed in Section 6.

6. Thrust Periodic Fluctuation Analysis

As analyzed in Section 5, the envelope of the airship has an impact on CRP performance. The closer the CRP is, the lower the thrust generated. This implies that a single propeller blade generates less thrust when it rotates closer to the envelope, causing a periodic thrust fluctuation, which produces a bending moment on the propeller shaft and can lead to structural fatigue in long endurance flight. Therefore, this section focuses on the analysis of envelope interference on single propeller blades.

In the case of a four-blade propeller at the start of rotation, as shown in Figure 20, thrust generated by each blade is different (Figure 20a). The bending moment generated by each blade does not offset each other (Figure 20b), leading to more stress on the motor.

The thrust of each propeller blade in a propeller is investigated, and propellers with different longitudinal positions are compared, as shown in Figure 21.

The periodic load is mainly observed when the propeller is at the front of the envelope. The periodic fluctuation is not caused by blade overlap, as the frequency is about the same as the rotation rate and the fluctuation is evenly distributed across the four blades, proving this fluctuation is the result of the envelope interference. The thrust of propeller blades with different lateral positions are also compared, but lateral distance to the envelope does not produce an obvious difference in the periodic fluctuation.

Figure 21 indicates that the magnitude of such periodic thrust fluctuation is dependent on the position of the CRP relative to the envelope. The difference between the maximum thrust and minimum thrust of propeller blades in the periodic fluctuation can be used to describe the magnitude of envelope interference, which can be calculated with Equation (11).

$$\Delta T_b = \max(T_{b1}, T_{b2}, T_{b3}, T_{b4}) - \min(T_{b1}, T_{b2}, T_{b3}, T_{b4}) \quad (11)$$

Figure 22 shows the magnitude of the periodic thrust fluctuation in relation to the propeller position.

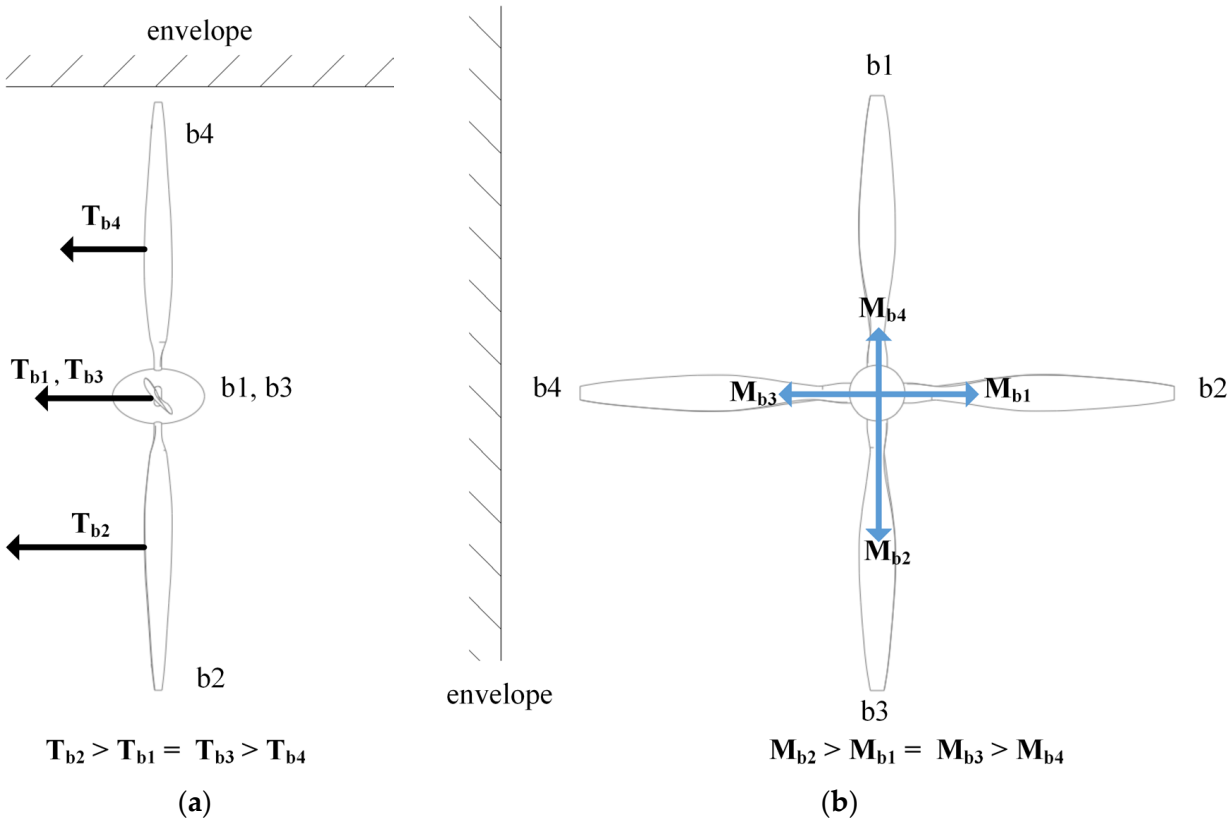


Figure 20. Thrust and bending moment generated by each blade (labeled *b*1~*b*4), with blade positions shown at the start of rotation: (**a**) top view of thrust generated by each blade (T_{b1}~T_{b4}); (**b**) front view of bending moment generated by each blade (M_{b1}~M_{b4}).

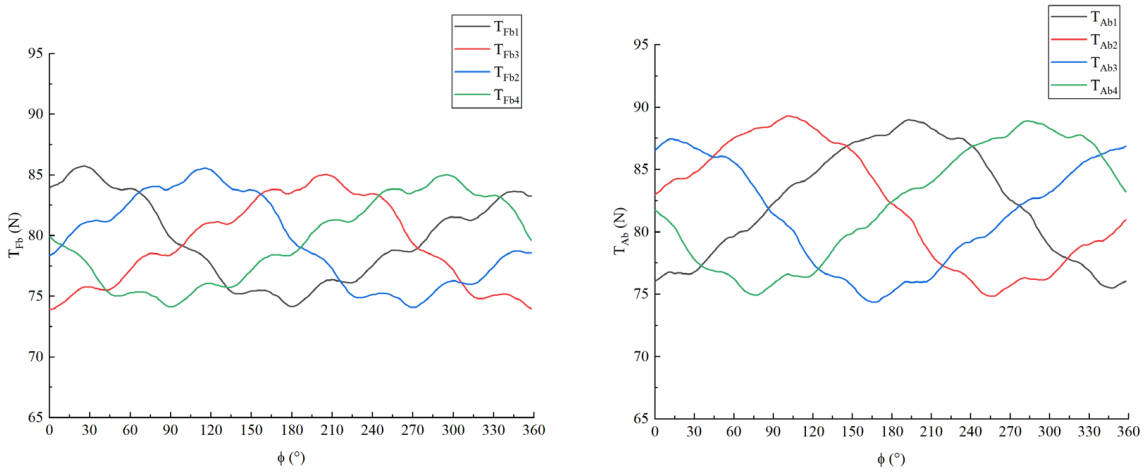


Figure 21. *Cont.*

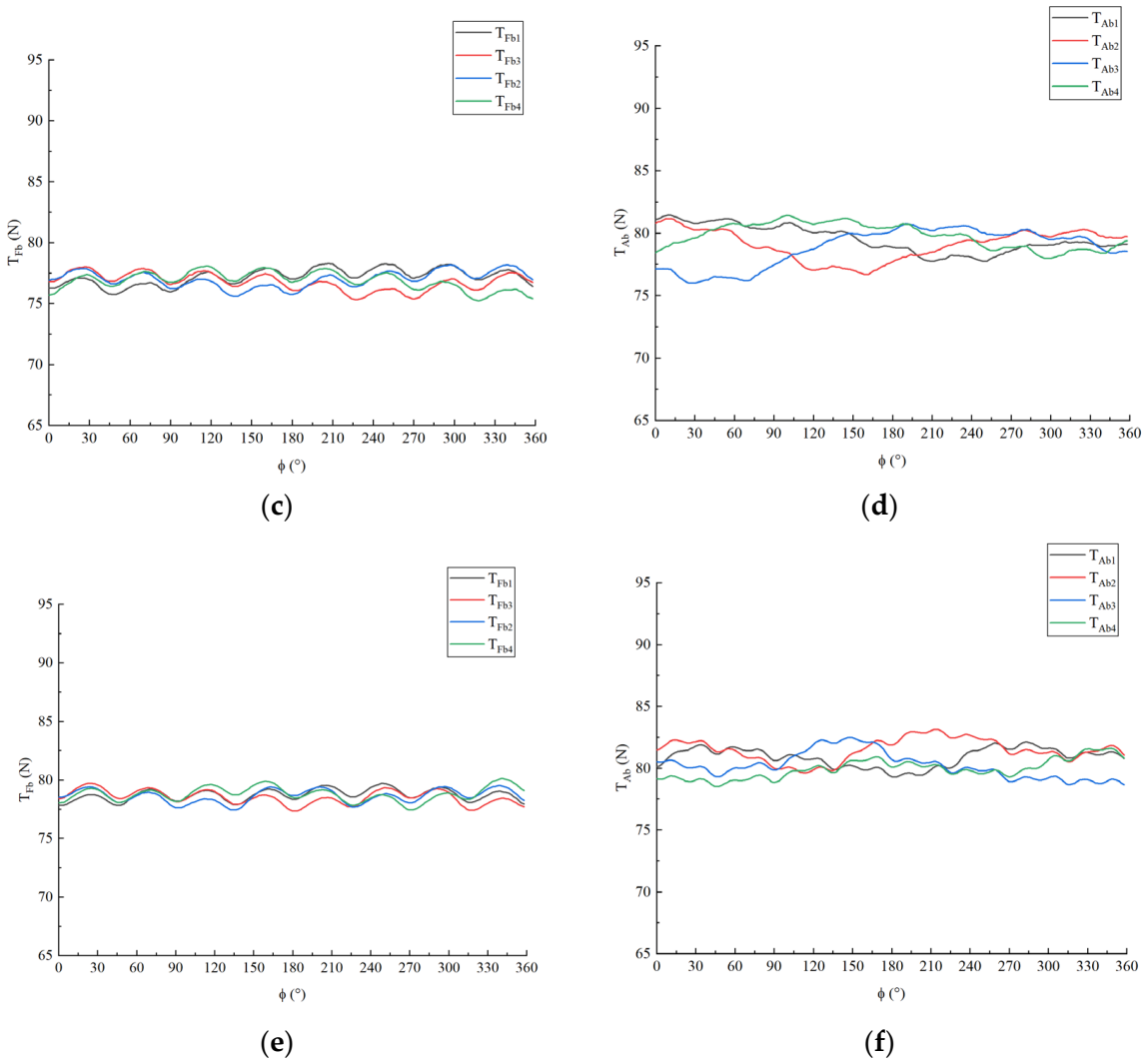


Figure 21. Thrust generated by the blades of the front propeller (T_{Fb1}~T_{Fb4}) and aft propeller (T_{Ab1}~T_{Ab4}), at b = 0.4: (**a**) thrust of front propeller, at a = 0.20; (**b**) thrust of aft propeller, at a = 0.20; (**c**) thrust of front propeller, at a = 0.45; (**d**) thrust of aft propeller, at a = 0.45; (**e**) thrust of front propeller, at a = 0.60; (**f**) thrust of aft propeller, at a = 0.60.

The magnitude of periodic thrust fluctuation in the front propeller and the aft propeller follows a similar trend, with a small difference in magnitude. In both propellers, the magnitude of fluctuation remains steady, with different lateral positions (b), but changes drastically at different longitudinal positions (a). The magnitude of fluctuation is insignificant when the propeller is at the middle and rear part of the envelope (a = 0.45 and a = 0.60), where the fluctuation is more a result of CRP overlap interference rather than envelope interference. Meanwhile, the fluctuation is more obvious and potentially detrimental when the propeller is at the front part of the envelope (a = 0.20), where the magnitude of fluctuation can reach 12~14 N (about 14~17% of the average thrust generated on a single blade). There are sudden and irregular changes in the magnitude of fluctuation at a = 0.60, because the fluctuation at this position is so insignificant that ΔT_{Fb} and ΔT_{Ab} are caused more by deviation introduced by the unsteady airflow rather than periodic thrust fluctuation.

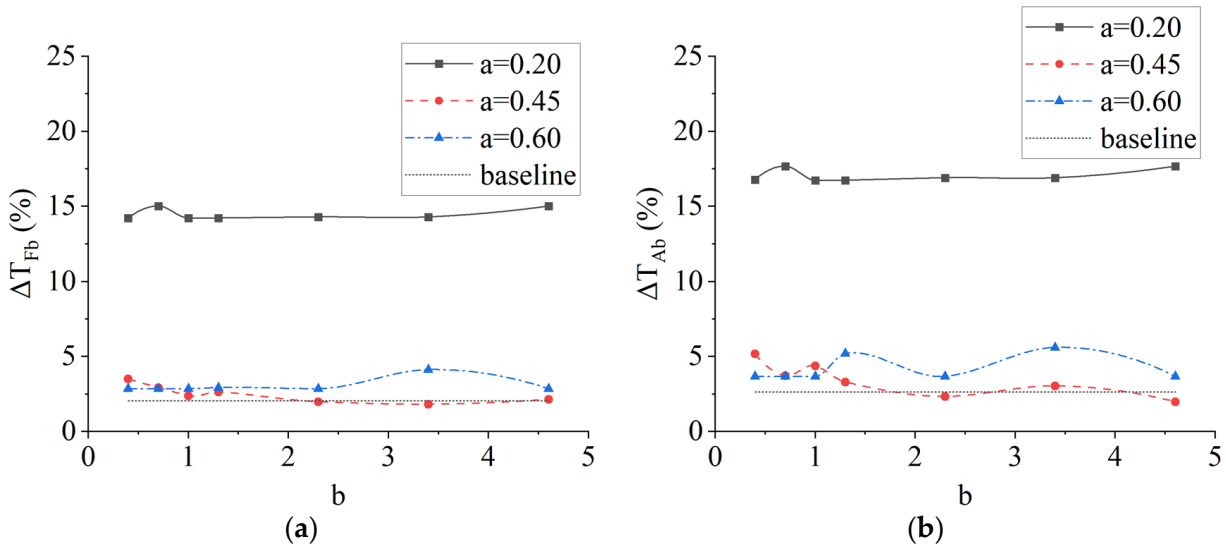


Figure 22. Magnitude of periodic thrust fluctuation on the blades of the front propeller and aft propeller as the percentage of the average thrust on a single blade (ΔT_{Fb} and ΔT_{Ab}) at different longitudinal and lateral positions (a and b): (**a**) thrust fluctuation of the front propeller; (**b**) thrust fluctuation of the aft propeller.

7. Discussion

This paper did not include physical experiment data for the following reasons: Firstly, the stratospheric airship is large in scale and operate at near-space altitude, making the multiple experiments needed in this paper too costly and complicated. Secondly, the main focus of this paper is to provide advice on propeller layout design on a qualitative level, where specific data on propeller performance is not necessary.

Therefore, a CFD simulation method, which is configured to reflect the typical operation conditions of stratospheric airships, is adopted to confirm the existence and significance of envelope interference.

In future research, it is possible to perform scaled experiments under sea level atmosphere to qualitatively confirm the findings in this paper. If exact magnitude of interference is needed for the optimization of the airship layout design, test flight experiments can be performed for more accurate and quantitative data on propeller performance.

8. Conclusions

By simulating the performance of an isolated CRP, comparing the performance of CRP at different relative positions to the airship envelope, and analyzing the effect of envelope interference on single propeller blades, the following conclusions are reached.

1. For the two propellers in a CRP, the aerodynamic thrust, torque, efficiency, and thrust of each propeller blade fluctuate periodically due to the overlap of the two propellers. This fluctuation is insignificant in magnitude but should be distinguished from the fluctuation caused by envelope interference.
2. The airship envelope has a noticeable effect on CRP performance. Propellers at the middle part of the envelope have a more significant total thrust drop than the propellers at the rear part of the envelope, while the total thrust of propellers at the front part of the envelope is almost not influenced by the envelope. The closer the propeller is to the envelope, the lower the total thrust. The torque and efficiency show the same trend as the thrust.
3. The thrust generated by each propeller blade fluctuates periodically due to the interference of the airship envelope during rotation. The magnitude of the fluctuation

is more significant when positioned at the front part of the envelope, reaching 14% of the total force, but is almost indistinguishable from the background fluctuation caused by propeller overlap interference when positioned at the middle and rear part of the envelope.

The position of the CRP has two main implications on CRP performance: total thrust and periodic thrust fluctuation. Total thrust is in proportion to the efficiency of the propeller, and periodic thrust fluctuation is generally detrimental to the structural integrity of the propeller and motor. When positioned at the front part of the envelope, the CRP's total thrust is almost not interfered by the envelope, but the magnitude of the periodic thrust fluctuation reaches its maximum. When the propeller is positioned at the rear part of the envelope, the CRP's total thrust is lowered by interference. But with more lateral distance to the envelope, the interference can be eliminated. The magnitude of the periodic thrust fluctuation is smaller than that of the propeller at the front part of the envelope. When the propeller is positioned at the middle part of the envelope, the CRP total thrust is even lower, which means more lateral distance is needed to reduce interference. But the magnitude of the periodic thrust fluctuation is at minimum.

For CRPs at the middle and rear part of the envelope, the efficiency and total thrust decreases are insignificant. The decrease can also be minimized by giving the CRP more lateral distance to the envelope. However, for CRPs at the front part of the envelope, the periodic thrust fluctuation on propeller blades are more obvious and detrimental. Therefore, it is advisable to place CRPs at the middle or rear part of the envelope as far as the scope of this paper is concerned.

Author Contributions: Conceptualization, G.T. and L.J.; methodology, L.J. and B.X.; software, L.J.; validation, G.T. and L.J.; formal analysis, J.Z.; investigation, J.Z.; resources, B.X. and J.C.; data curation, J.Z.; writing—original draft preparation, J.Z.; writing—review and editing, J.Z. and G.T.; visualization, J.Z.; supervision, C.X. and G.T.; project administration, C.X. and G.T.; funding acquisition, C.X. and G.T. All authors have read and agreed to the published version of the manuscript.

Funding: This research received no external funding.

Data Availability Statement: The authors confirm that the data supporting the findings of this study are available within this article. Further inquiries can be directed to the corresponding author.

Conflicts of Interest: The authors declare no conflicts of interest.

Abbreviations

The following abbreviations are used in this manuscript:

CRP	Contra-rotating propeller
CFD	Computational fluid dynamic
FVM	Finite volume method

References

1. D'Oliveira, F.A.; Melo, F.C.L.d.; Devezas, T.C. High-Altitude Platforms—Present Situation and Technology Trends. *J. Aerosp. Technol. Manag.* **2016**, *8*, 249–262. [CrossRef]
2. Colozza, A.; Dolce, J. *Initial Feasibility Assessment of a High Altitude Long Endurance Airship*; NASA/CR-2003-212724; National Aeronautics and Space Administration Glenn Research Center: Cleveland, OH, USA, 2003.
3. Cheng, J.S.; Ding, J.B.; Gong, X.R.; Wang, S.; Jiang, B.Y.; Nie, Y. Dynamic characteristics of flexible hull-propulsion systems in stratospheric airships: FEA and experimental study. *Aerosp. Sci. Technol.* **2025**, *165*, 110529. [CrossRef]
4. Zhou, P.; Lin, Q.; Jing, Y. An introduction to electric thruster modeling for stratospheric airship. *Aerosp. Syst.* **2024**, *7*, 315–325. [CrossRef]
5. Riccio, E.; Alifano, F.; Baraniello, V.R.; Coiro, D. A Comprehensive Review of Propeller Design and Propulsion Systems for High-Altitude Pseudo-Satellites. *Appl. Sci.* **2025**, *15*, 8013. [CrossRef]

6. Mourousias, N.; Marinus, B.G.; Runacres, M.C. A novel multi-fidelity optimization framework for high-altitude propellers. *Aerosp. Sci. Technol.* **2024**, *153*, 109407. [CrossRef]
7. Gray, W.H. *Wind-Tunnel Tests of Single- and Dual-Rotating Pusher Propellers Having from Three to Eight Blades*; Langley Memorial Aeronautical laboratory: Lanley Field, VA, USA, 1942.
8. He, L.; Dou, M.; Wang, G. Research on Airscrew Electric Propulsion System for Stratosphere Airship. *Small Spec. Electr. Mach.* **2009**, *37*, 1–4.
9. Chen, S.; Wang, H.; Song, B. Modeling and Dynamic Simulation Study of Big Inertia Propulsion System of High Altitude Airship. In Proceedings of the 2011 2nd International Conference on Artificial Intelligence, Management Science and Electronic Commerce (AIMSEC), Zhengzhou, China, 8–10 August 2011; pp. 4065–4068.
10. Liu, P.; Duan, Z.; Ma, L.; Ma, R. Aerodynamics Properties and Design Method of High Efficiency-Light Propeller of Stratospheric Airships. In Proceedings of the 2011 International Conference on Remote Sensing, Environment and Transportation Engineering, Nanjing, China, 24–26 June 2011; pp. 8041–8044.
11. Liu, P.; Rong, M.; Duan, Z.; Ma, L. Ground wind tunnel test study of the propeller of stratospheric airships. *J. Aerosp. Power* **2011**, *26*, 1775–1781.
12. Wang, Y.; Liu, Z.; Tao, G. Numerical simulation of high altitude propeller's aerodynamic characteristics and wind tunnel test. *J. Beijing Univ. Aeronaut. Astronaut.* **2013**, *39*, 1102–1105.
13. Liu, X.; He, W. Performance Calculation and Design of Stratospheric Propeller. *IEEE Access* **2017**, *5*, 14358–14368. [CrossRef]
14. Xie, C.; Tao, G.; Wu, Z. Performance Prediction and Design of Stratospheric Propeller. *Appl. Sci.* **2021**, *11*, 4698. [CrossRef]
15. Tang, Z.; Liu, P.; Guo, H.; Yan, J.; Li, G. Two-Dimensional Moving Blade Row Interactions in a Stratospheric Airship Contra-Rotating Open Propeller Configuration. *Int. J. Aeronaut. Space Sci.* **2015**, *16*, 500–509. [CrossRef]
16. Chen, Y.; Liu, P.; Tang, Z.; Guo, H. Wind tunnel tests of stratospheric airship counter rotating propellers. *Theor. Appl. Mech. Lett.* **2015**, *5*, 58–61. [CrossRef]
17. Xie, C.; Tao, G.; Wu, Z. The study of spacing influence on the performance of Contra-Rotation-Propeller in stratospheric airship. *IOP Conf. Ser. Mater. Sci. Eng.* **2020**, *772*, 012066. [CrossRef]
18. Xie, C.; Tao, G.; Wu, Z. The study of rotate speed influence on the performance of Contra-Rotation-Propeller in stratospheric airship. *IOP Conf. Ser. Earth Environ. Sci.* **2021**, *714*, 042080. [CrossRef]
19. Hadipour, M.; Kamali, R. Experimental and Numerical Investigation of Propeller Propulsion System Behavior Considering the Ground Effect. *Unmanned Syst.* **2024**, *13*, 1143–1154. [CrossRef]
20. Xie, F.; Ye, Z. Drag Reduction for an Airship with Proper Arrangement of Propellers. *Chin. J. Aeronaut.* **2009**, *22*, 575–582. [CrossRef]
21. Konus, M.F.; Savaş, O. Rotor Vortex Wake in Close Proximity of Walls in Hover. *J. Am. Helicopter Soc.* **2014**, *61*, 042003.
22. Chen, X.; Chen, H.; Chen, K.; Tang, J. Study on the Aerodynamics Interaction Between Propeller and Stratospheric Airship with Multi-propeller Layout. In *Advances and Challenges in Advanced Unmanned Aerial Systems: Selected Contributions of ICAUAS 2023*; Liu, Z., Li, R., He, X., Zhu, Z., Eds.; Springer Aerospace Technology: Singapore, 2024; pp. 257–268.
23. Oh, K.-J.; Kang, S.-H. Numerical calculation of the viscous flow around a rotating marine propeller. *KSME J.* **1992**, *6*, 140–148. [CrossRef]
24. Ramírez, L.; Foulquié, C.; Nogueira, X.; Khelladi, S.; Chassaing, J.-C.; Colominas, I. New high-resolution-preserving sliding mesh techniques for higher-order finite volume schemes. *Comput. Fluids* **2015**, *118*, 114–130. [CrossRef]
25. Moukalled, F.; Mangani, L.; Darwish, M. *The Finite Volume Method in Computational Fluid Dynamics*; Springer: Cham, Switzerland, 2016.
26. Menter, F. Zonal Two Equation k-w Turbulence Models for Aerodynamic Flows. In Proceedings of the 23rd Fluid Dynamics, Plasmadynamics, and Lasers Conference, Orlando, FL, USA, 6–9 July 1993.
27. Menter, F.; Kuntz, M.; Langtry, R.B. Ten years of industrial experience with the SST turbulence model. *Heat Mass Transf.* **2003**, *4*, 625–632.
28. An, W.; Li, W.; Wang, H. Multi-objective optimization design of envelope shape of a certain airship with deviations considered. *J. Northwestern Polytech. Univ.* **2007**, *25*, 56–60.
29. Funk, P.; Lutz, T.; Wagner, S. Experimental investigations on hull-fin interferences of the LOTTE airship. *Aerosp. Sci. Technol.* **2003**, *7*, 603–610. [CrossRef]
30. Mathur, S. Unsteady Flow Simulations Using Unstructured Sliding Meshes. In Proceedings of the Fluid Dynamics Conference, Colorado Springs, CO, USA, 20–23 June 1994.
31. Pan, D.; Chao, M.-J.; Chien, S.K. Euler Computations of Rotor Flows on Unstructured Rotating Meshes. *J. Aircr.* **2001**, *38*, 672–679. [CrossRef]
32. Blades, E. A Sliding Interface Method for Unsteady Unstructured Parallel Flow Simulations. Ph.D. Dissertation, Mississippi State University, Starkville, MS, USA, 2004.

33. Wei, J.; Sha, Y.-B.; Hu, X.-Y.; Yao, J.-Y.; Chen, Y.-L. Aerodynamic Numerical Simulation Analysis of Water–Air Two-Phase Flow in Trans-Medium Aircraft. *Drones* **2022**, *6*, 236. [CrossRef]
34. National Geophysical Data Center. U.S. standard atmosphere (1976). *Planet. Space Sci.* **1992**, *40*, 553–554. [CrossRef]
35. Stuermer, A.; Yin, J. Aerodynamic and Aeroacoustic Installation Effects for Pusher-Configuration CROR Propulsion Systems. In Proceedings of the 28th AIAA Applied Aerodynamics Conference, Chicago, IL, USA, 28 June–1 July 2010.
36. Stuermer, A.W.; Akkermans, R.A. Validation of Aerodynamic and Aeroacoustic Simulations of Contra-Rotating Open Rotors at Low-Speed Flight Conditions. In Proceedings of the 32nd AIAA Applied Aerodynamics Conference, Atlanta, GA, USA, 26–20 June 2014.

Disclaimer/Publisher's Note: The statements, opinions and data contained in all publications are solely those of the individual author(s) and contributor(s) and not of MDPI and/or the editor(s). MDPI and/or the editor(s) disclaim responsibility for any injury to people or property resulting from any ideas, methods, instructions or products referred to in the content.